crystals

MDPI

Article

Carbochlorination Reduction Process of Waelz ZnO: Characterization of Resulting ZnO-Based Oxides

Lorena Alcaraz [1,*,†], Belén Sotillo [2,*,†], Paloma Fernández [2] and Félix A. López [1]

[1] Centro Nacional de Investigaciones Metalúrgicas (CENIM), Consejo Superior de Investigaciones Científicas (CSIC), Avda. Gregorio del Amo 8, 28040 Madrid, Spain; f.lopez@csic.es
[2] Department of Materials Physics, Faculty of Physics, Complutense University of Madrid, Plaza de Ciencias 1, 28040 Madrid, Spain; arana@ucm.es
* Correspondence: alcaraz@cenim.csic.es (L.A.); bsotillo@ucm.es (B.S.)
† These authors contributed equally to this work.

Abstract: Zinc-based oxides are the main products obtained after the Waelz process, a metallurgical method used industrially for the treatment of electric arc furnaces. These oxides have certain impurities in their composition, which can be a disadvantage. Carbochlorination reduction reactions have proven to be useful in eliminating certain impurities (especially Pb) through thermal treatments. In this work, a method for purifying Waelz oxide through carbochlorination reduction reactions is presented. Several experiments have been conducted with the aim of obtaining samples with potential end applications. A deep characterization of the purified oxides has been performed by means of X-ray microanalysis, X-ray diffraction, Raman spectroscopy, and cathodoluminescence. These measurements indicate the presence of ZnO and $ZnFe_2O_4$ in different proportions, depending on the different amounts of reducing and chlorinating agents used.

Keywords: ZnO; $ZnFe_2O_4$; carbochlorination reduction; purification; cathodoluminescence

Academic Editor: Pier Carlo Ricci

Received: 14 February 2025
Revised: 24 March 2025
Accepted: 25 March 2025
Published: 28 March 2025

Citation: Alcaraz, L.; Sotillo, B.; Fernández, P.; López, F.A. Carbochlorination Reduction Process of Waelz ZnO: Characterization of Resulting ZnO-Based Oxides. *Crystals* **2025**, *15*, 326. https://doi.org/10.3390/cryst15040326

1. Introduction

Zinc is the third most significant non-ferrous metal, following aluminum and copper, owing to its effectiveness in protecting steel against corrosion. In fact, approximately 50% of globally produced zinc is utilized for galvanizing steel [1]. When steel scrap reaches the end of its lifespan, it is commonly recycled through a scrap-based steelmaking process, such as an electric arc furnace (EAF) [2].

The Waelz process is a pyrometallurgical technology primarily used for the treatment and recycling of steelmaking dust generated in electric arc furnaces during steel production from ferrous scrap. Its main objective is to recover zinc oxides and other metals present in these steel industry residues [3].

The process takes place in an inclined rotary kiln, where the steelmaking dust is mixed with a reducing agent (such as coal, coke, or petroleum coke) and fluxes (such as lime or dolomite). The mixture is then subjected to temperatures between 1000 and 1300 °C, promoting the selective volatilization of zinc and other non-ferrous metals. At these high temperatures, zinc oxide (ZnO) is reduced to gaseous metallic zinc (Zn). The zinc, along with other volatile metals (such as lead and cadmium), evaporates and is carried away with the exhaust gases. At the upper section of the system, the zinc vapors cool and reoxidize into zinc oxide (ZnO), which is then captured in filters and referred to as Waelz oxide (WO). A typical WO composition includes approximately 66 wt% Zn, 0.15% Cd, 0.9% Fe, 2.7% Pb, 1.3% Na, 4% Cl, and 0.1% Mn. Mineralogically, WO consists of zincite (ZnO), halite

(NaCl), franklinite ($ZnFe_2O_4$), and other mineral phases [3,4]. WO serves as a primary raw material for the production of refined zinc. It is also used in the manufacturing of pigments, fertilizers, and ceramic materials, among other applications.

However, certain applications of ZnO require high purity, making it necessary to refine WO to increase its zinc content while reducing impurity levels.

To address this, ongoing research is focused on improving the purity of WO. This study investigates a carbothermic reduction and chlorination process to reduce iron and other volatile metal contents, primarily lead (Pb).

The carbochlorination process [5] is a process in which a metal oxide is converted to its corresponding metal chloride in the presence of carbon and chlorine gas. From a thermodynamic perspective, carbon works as a reducing agent and reduces the required reaction temperature. From a kinetics standpoint, it has been observed that direct contact between the metal oxides and carbon is not essential for effective chlorination. This has led to the conclusion that the carbochlorination reaction occurs through the presence of gaseous intermediates. It is believed that carbon promotes the formation of these intermediates due to its catalytic activity, which allows for the generation of highly reactive gas intermediates.

Previous studies [6] have reported that

$$ZnO{\cdot}Fe_2O_3 \rightarrow ZnO + Fe_2O_3 \quad (1)$$

Then, Fe_2O_3 is reduced to Fe:

$$Fe_2O_3 + 3C \rightarrow 3Fe + 3CO \quad (2)$$

The intermediate reactions are described by the following reactions in the temperature range between 700 and 1200 °C:

$$3Fe_2O_3 + CO \rightarrow 2Fe_3O_4 + CO_2 \quad (3)$$

$$Fe_3O_4 + CO \rightarrow 3FeO + 3CO_2 \quad (4)$$

$$FeO + CO \rightarrow Fe + 3CO_2 \quad (5)$$

Iron oxides are reduced by carbothermic reduction, and the zinc produced from the reduction of ZnO is released immediately in gaseous form, while the Fe_2O_3 is reduced through the sequence $Fe_2O_3 \rightarrow Fe_3O_4 \rightarrow FeO \rightarrow Fe$, confirming the above equations.

In the present work, we describe an effective process to purify the Waelz oxide using carbochlorination reduction reactions. Several conditions were assessed to eliminate most impurities present in the initial sample. All samples obtained were deeply characterized. The final purified recovered samples were ZnO and $ZnFe_2O_4$, two stoichiometries with potential applications.

2. Materials and Methods

2.1. Obtention of the Samples

The feed material used in this study is a Waelz oxide, which was subjected to an air classification process. This treatment involves separating the material into different fractions based on size, shape, and density to improve its chemical composition by selectively eliminating fine fractions that are enriched with impurities. The starting material (WON) was provided by a company specializing in WO production.

The WON material was then subjected to thermal treatments in an oven in the presence of chlorinating and reducing agents. To analyze the influence of several experimental conditions on the purification of the WON, a series of tests were conducted as outlined in

Table 1. Two different reducing agents (fluid polyethylene terephthalate (fluid PET) and anthracite) were used for the tests, and zinc chloride ($ZnCl_2$) was used as a chlorinating agent. The final product analyzed is the solid residue collected after the thermal treatments.

Table 1. Carbochlorination reduction tests conducted in the present work.

$ZnCl_2$ (wt%)	Reducing Agent	C (wt%)	Time (h)	Sample Notation
3.5	Fluid PET	5	1	M1_1h
			2	M1_2h
			3	M1_3h
2	Fluid PET	3	1	M2
		5		M3
	Anthracite	3		M4
		5		M5
3.5	Anthracite	3		M6
		5		M7

Thus, a representative amount of the initial sample was mixed and homogenized with $ZnCl_2$ and the reducing agent. For a fixed amount of reducing and chlorinating agent, the influence of the reaction time was evaluated by varying it between 1 h and 3 h. After the optimization of the reaction time, carbochlorination reactions were carried out as previously described according to Equations (1)–(5). It should be noted that all carbochlorination reduction tests were carried out at 850 °C.

2.2. Characterization of the Samples

Morphological characterization was performed using scanning electron microscopy (SEM) with an FEI Inspect microscope (FEI Company, Eindhoven, The Netherlands) working at 15–20 kV. Structural characterization of the samples was carried out via micro-Raman measurements at room temperature with a Horiba Jobin Yvon LabRAM HR800 (Horiba JobinYvon, Villeneuve d'Ascq, France) confocal microscope. Raman spectra were recorded under excitation with the 632.8 nm line of a He-Ne laser. A Synapse charge-coupled device (CCD) detector (Horiba JobinYvon, Villeneuve d'Ascq, France) was used to collect the scattered light dispersed by a 600 lines/mm grating. The spectral resolution of the system used was 1.5 cm^{-1}. Further structural characterization was performed by means of X-ray diffraction (XRD) measurements, performed with a Bruker D8 Advance A25 diffractometer (Bruker, Karlsruhe, Germany) using Cu-Kα radiation, with a step in 2θ of 0.05°. The diffractometer is equipped with a Cu tube in the th/th configuration, Bragg–Bretano optics, and a LynxEye SSD160-2 position sensitive detector (Bruker, Billerica, UK).

Cathodoluminescence (CL) investigations were performed at room temperature with a HITACHI S2500 SEM (Hitachi High Technologies Corporation, Tokyo, Japan), using an accelerating voltage of 15 kV. Spectra were recorded with a CCD camera HAMAMATSU PMA-12 (spectral range 200–900 nm) coupled to an optical fiber.

Chemical composition was determined by flame atomic absorption spectrometry (AAS) using a ContrAA 700 (Analytik Jena AG, Jena, Germany). For this, 0.1 g of each sample was dissolved with 5 mL of aqua regia (HNO_3:HCl, 1:3) and subjected to heating during the previously determinate time. The liquid volume for each test was kept constant by the addition of MilliQ water. Then, the digested mixture was transferred to a 100 mL flask and brought to volume using MilliQ water. High-resolution continuous source atomic absorption spectrometry (HR-AAS CS) and a CCD detector with a UV-VIS wavelength range (Analytik Jena AG, Jena, Germany) were utilized for the determination of lithium, fluorine, and phosphorus in the acidic aqueous solutions. Element distribution was determined using energy dispersive X-ray microanalysis (EDX) performed with a SEM Hitachi

TM3000 (Hitachi High Technologies Corporation, Tokyo, Japan) working at 15 kV, with an EDX detector Bruker QUANTAX 70 (Bruker, Berlin, Germany).

Magnetic measurements were registered using a PPMS-14 T (Physical Property Measurement System) (Quantum Design, San Diego, CA, USA) at room temperature. Magnetization as a function of the applied magnetic field was determined using vibrating sample magnetometry (VSM).

3. Results and Discussion

3.1. Characterization of the Initial Waelz Oxide Sample

The chemical composition of WON is provided in Table 2. The chemical composition of WON and the other samples obtained in the purification process was determined by atomic absorption and ion chromatography. Prior to analysis, the samples were digested in a Berghof SW-X digestion system. For this, 500 mg of each sample was treated with 7 mL of HNO_3 (70%) and 1 mL of HF (49%) at 210 °C and 35 bar of pressure. Once in solution, the metal contents were determined by atomic absorption spectroscopy using a ContraA800D instrument from Analytik Jena. Additionally, the concentration of chloride ions was determined by ion exchange chromatography using an advanced ion chromatograph (Metrohm AG, Herisau, Switzerland).

Table 2. Chemical composition of the initial Waelz oxide sample (WON).

Element	Zn	Fe	Pb	Cd	Mn	Cl
wt%	72.4	0.45	2.64	0.17	0.01	5.8

The characterization results indicate that WON exhibits a higher ZnO content and reduced concentrations of impurities (Fe, Pb, etc.) compared to WO. The mean particle size, determined by laser diffraction analysis, was 3.7 μm.

Pb, Fe, and Cd were found as impurities, according to the typical composition of the Waelz oxide samples [2]. However, other impurities in lower concentrations were also detected. Figure 1a presents the XRD measurements of the starting powder. It is clear that the most intense maxima can be associated with the ZnO wutzite structure (Powder Diffraction File (PDF-2, [7]) no. 00-036-1451). Along with the ZnO maxima, diffractions related to different lead oxides, lead chlorides, iron chlorides, and iron oxides can be identified, as shown in Figure 1b. This is in agreement with the impurities detected in the AAS measurements. Finally, Figure 1c shows the SEM image obtained for the WON sample. Particle agglomerates can be appreciated, presenting the particles' hexagonal habits, in agreement with the wurtzite structure of ZnO.

The elemental distribution maps and energy-dispersive X-ray spectroscopy analysis of the WON powder are presented in Figure 2. This analysis shows that the sample is fundamentally composed of Zn. Despite that, some impurities distributed throughout the sample were also found. Cl, Pb, and Fe were detected as principal impurities, in good agreement with the obtained results from the AAS measurements. As can be appreciated, the impurities are located and concentrated in particle agglomerates, probably between ZnO particles.

The cathodoluminescence spectrum for the initial sample (Figure 3a) shows a broad intense emission band, centered approximately at 510 nm, and another band at 385 nm. The obtained CL emission spectrum is typical of ZnO and can be attributed to band-edge emission and defects-related emission [8]. These results could indicate that the impurities found would be outside the ZnO matrix since the presence of transition metals exerts a stronger influence on the ZnO host matrix, leading to much quenching of the luminescence [9].

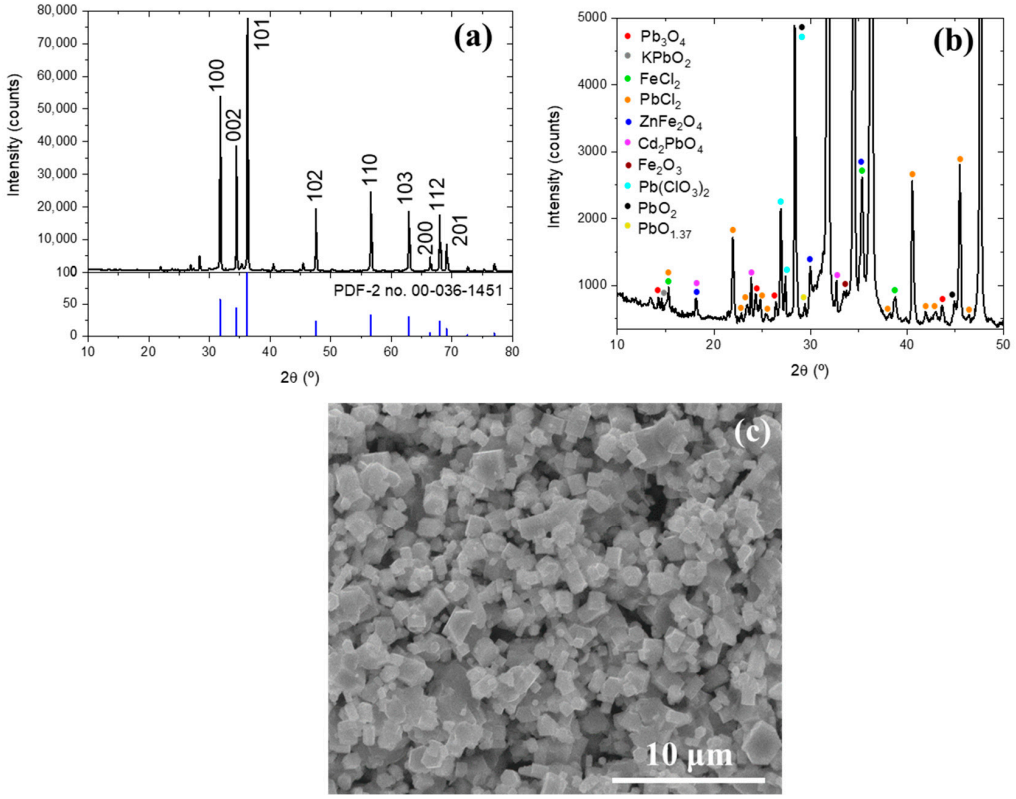

Figure 1. XRD measurements performed on the starting Waelz oxide: (**a**) ZnO-related XRD reflections; (**b**) zoom of the maxima between 2θ = 10° and 50°. Identified compounds are Pb_3O_4 (PDF-2 no. 01-071-0561, red circles); $KPbO_2$ (PDF-2 no. 00-021-0990, gray circles); $FeCl_2$ (PDF-2 no. 01-070-1634, green circles); $PbCl_2$ (PDF-2 no. 01-084-1177, orange circles); $ZnFe_2O_4$ (PDF-2 no. 01-077-0011, blue circles); Cd_2PbO_4 (PDF-2 no. 00-038-1153, magenta circles); Fe_2O_3 (PDF-2 no. 01-084-0311, brown circles); $Pb(ClO_3)_2$ (PDF-2 no. 00-038-1085, cyan circles); PbO_2 (PDF-2 no. 00-037-0517, black circles); $PbO_{1.37}$ (PDF-2 no. 00-027-1202, yellow circles). (**c**) SEM image for the initial Waelz oxide sample.

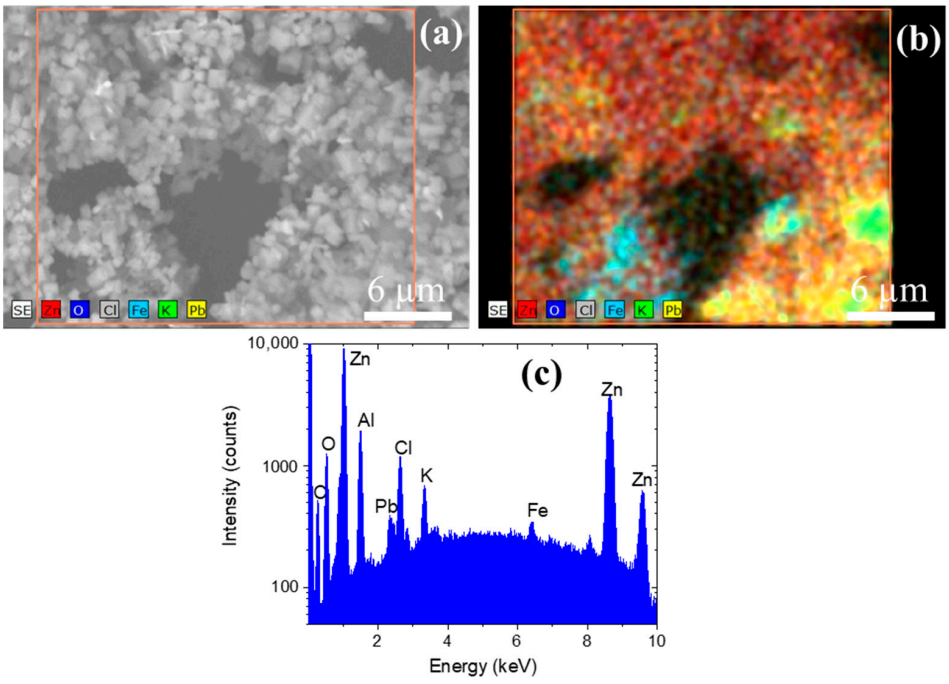

Figure 2. (**a**) Backscattered electron (BE) image, (**b**) EDX element distribution maps (Zn in red, Cl in gray, Fe in light blue, K in green, and Pb in yellow), and (**c**) EDX spectrum for the initial WON sample. Al signal observed in the spectrum comes from the sample holder.

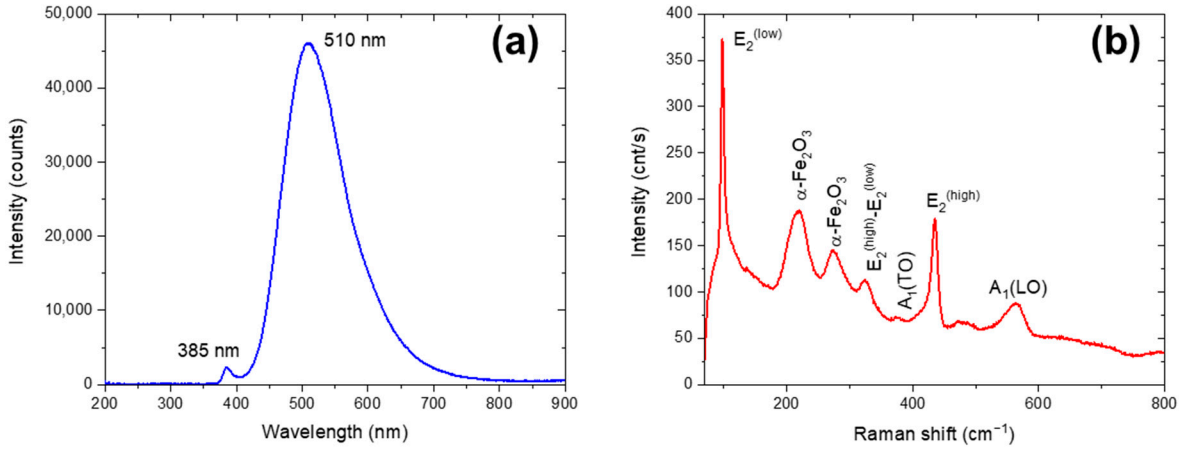

Figure 3. (**a**) Cathodoluminescence and (**b**) micro-Raman spectra for the initial WON sample.

The spectrum registered by micro-Raman spectroscopy (Figure 3b) exhibits several bands attributable to the ZnO [10]. The zero-order optical phonons in the ZnO wurtzite structure are given by $\Gamma_{opt} = A_1 + 2B_1 + E_1 + 2E_2$ [10]. The A1 and E1 modes are polar and split into a transverse optical mode (TO) and a longitudinal optical mode (LO). The E_2 mode consists of low $E_2^{(low)}$ and high $E_2^{(high)}$ frequency phonon modes, where $E_2^{(high)}$ is associated with the vibration of oxygen atoms, and $E_2^{(low)}$ is related to heavy Zn sublattices. On the other hand, the B_1 modes are not Raman active [10]. Then, in the Raman spectrum, the ZnO vibrations identified display sharp peaks at 97 and 435 cm^{-1} related to $E_2^{(low)}$ and $E_2^{(high)}$, respectively; the $E_2^{(high)}$–$E_2^{(low)}$ mode at 324 cm^{-1} (with A_1 symmetry); the A_1(TO) mode at 375 cm^{-1}; and the A_1(LO) mode at 574 cm^{-1}.

However, some bands, due to the vibration modes of the α-Fe_2O_3 compound, are also observed [11]. The peaks located at around 217 cm^{-1} and 274 cm^{-1} could be assigned to the A_{1g} and E_g modes, respectively [12]. These peaks are characteristic of the hematite structure.

3.2. Effect of the Reaction Time

The SEM micrographs of the samples obtained after the thermal treatment of the WO at 850 °C using a fixed amount of reducing agent as well as chlorinating agent (see Table 1) for different reaction times are shown in Figure 4. Particle agglomerates are visible in all of the images, with a partial sintering, as a consequence of the calcination process. In the case of the sample treated for 1 h (see Figure 4a), hexagonal crystals with a polyhedral morphology can be observed, typical of ZnO samples and similar to the original WON sample. However, as the reaction time increases (see Figure 4b,c), more spherical morphologies begin to appear. This result could be derived from the sintering process that also occurred during the thermal treatment carried out.

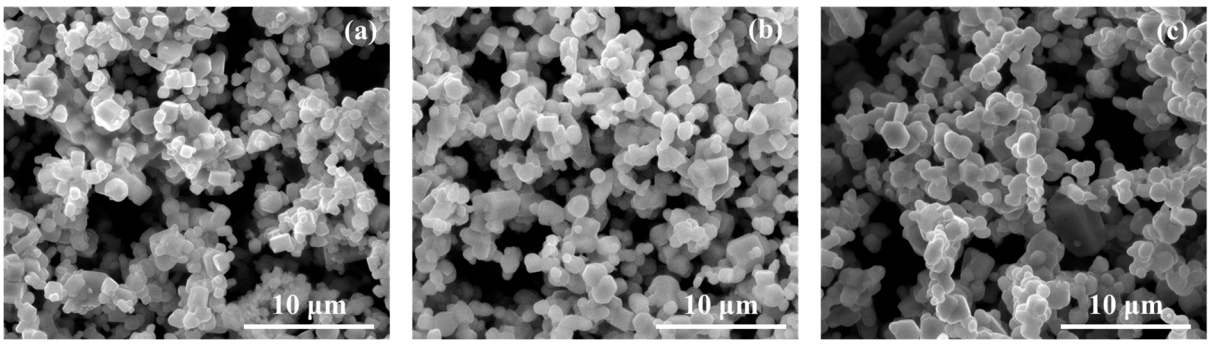

Figure 4. SEM images obtained for the samples treated at 850 °C for (**a**) 1 h, (**b**) 2 h, and (**c**) 3 h.

Elemental distribution maps plotted using Zn-K_α and Fe-K_α were obtained for each sample (see Figure 5a–c), which reveal areas with a non-homogeneous distribution of Fe. No additional impurities were detected within the sensitivity of the measurements. The Raman spectra for the three samples (Figure 5d–f) revealed the presence of ZnO-related modes (same as those described before; the origin is again indicated in the figure), whereas the modes associated with α-Fe_2O_3 disappeared. Additionally, a band centered at 650 cm^{-1} can be attributed to the $ZnFe_2O_4$ phase [13,14]. Finally, XRD measurements (Figure 5g–i) confirmed the disappearance of most of the XRD reflections related to lead oxides, lead chlorides, and iron chlorides, whereas the maxima associated with the $ZnFe_2O_4$ phase were still present.

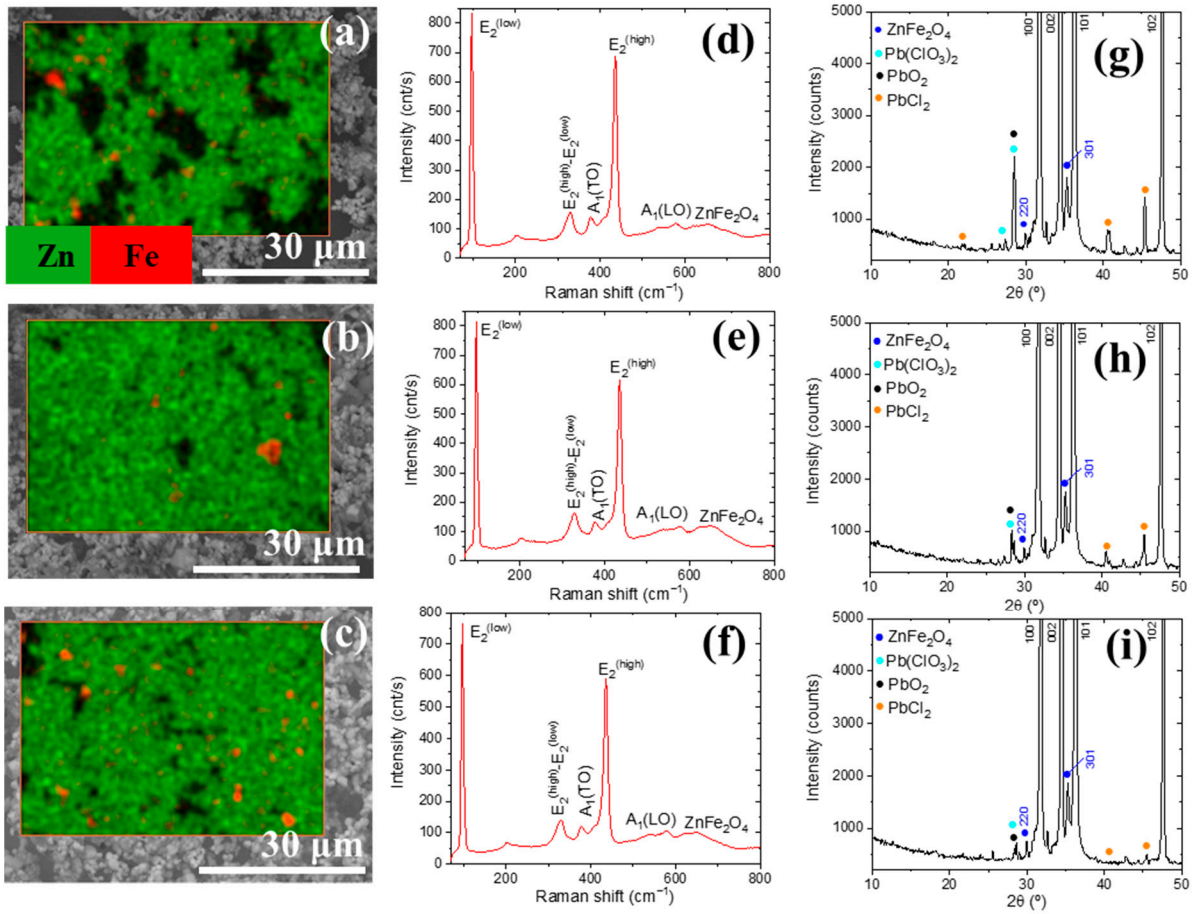

Figure 5. Element distribution maps of Zn-K_α (green) and Fe-K_α (red) for the thermal samples treated at different reaction times: (**a**) 1 h; (**b**) 2 h; (**c**) 3 h. (**d**–**f**) shows the Raman spectra for the same samples, whereas (**g**–**i**) presents the XRD patterns between 2θ = 10° and 50°.

Deeper information about the samples can be obtained from the CL measurements, as they are more sensitive to small concentrations of impurities in the ZnO lattice. The comparative CL spectra for the samples treated at different reaction times and starting samples are shown in Figure 6a. For the untreated WON sample, two emission maxima centered at around 385 nm and 510 nm, attributed to the band-edge emission and defects-related emission of ZnO, respectively [15,16], are detected. However, in the CL spectra for the M1_1h, M2_2h, and M3_3h samples, a shift of the two emissions is observed toward 391 nm and 524 nm. Additionally, the green emission band becomes narrower as the thermal treatment time increases. Finally, for the M1_2h and M1_3h samples, a new band appears at around 740 nm. All these observations are related to the incorporation of Fe into the ZnO network [17,18], and the narrower band at 524 nm can be associated with the

formation of the spinel phase $ZnFe_2O_4$ [14,19,20]. Figure 6b shows the deconvolution of the cathodoluminescence spectra for the initial WON sample and the samples obtained using lower and higher reaction times (Figure 6c,d, respectively). In the CL deconvolutions, for the original WON sample, the green band can be fitted with two Gaussians at 2.47 eV and 2.34 eV (Figure 6b). Using the same parameters for the Gaussians, M1_1h spectra (Figure 6c) can be fitted using an additional band at 2.36 eV (525 nm), ascribed to the spinel emission [19,20], which has a high emission efficiency. Finally, M1_3h (Figure 6d) can be fitted just employing the 2.36 eV. Then, the higher the reaction time is, the larger incorporation of Fe into the ZnO lattice, and a spinel formation is observed, which can be related to a more efficient diffusion of Fe atoms into the ZnO matrix over longer times. Considering this, along with the removal of most of the Pb observed in the EDX, the subsequent tests were carried out using 1 h of reaction time.

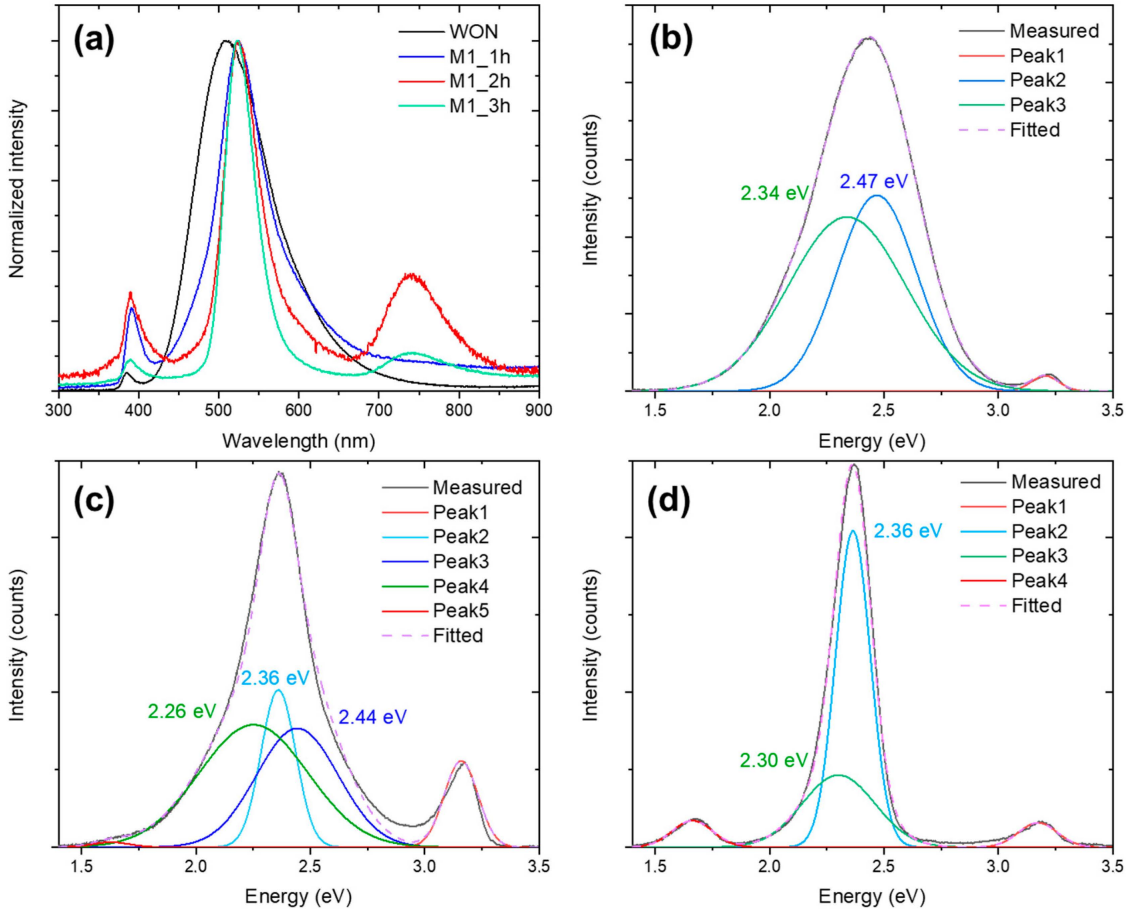

Figure 6. (**a**) Comparative spectra for the WON sample and the samples obtained at different reaction times; deconvoluted CL spectra for the initial WON (**b**), M1_1h (**c**), and M1_3h samples (**d**).

3.3. Carbochlorination Reduction Tests from Waelz Oxide

After the optimization of the reaction time, the influence of different types and amounts of reducing agent on carbochlorination reduction, as well as the effect of the chlorinating agent amount, was assessed. In order to perform this study, the amount of chlorinating agent was first fixed (2 wt% of $ZnCl_2$), while the reducing agent (fluid PET and anthracite) amount was varied (3 wt% and 5 wt%). Then, for the best reducing agent (anthracite), the chlorinating agent $ZnCl_2$ amount was increased to 3.5 wt%. For samples M2 to M7 detailed in Table 1, the chemical composition is determined from the AAS measurements. The results are shown in Table 3.

Table 3. Chemical composition of the obtained samples treated with different amounts of reducing agent and chlorinating agent (see Table 1 for the complete detail of the treatments).

Element/C wt%	M2	M3	M4	M5	M6	M7
Zn	73.74	74.23	78.29	71.67	70.71	67.21
Fe	0.61	0.77	0.57	0.52	0.51	0.52
Pb	0.01	0.57	0.10	0.54	0.03	0.67
Cd	0.01	-	0,01	-	-	-
Mn	0.06	0.08	0.06	0.06	0.06	0.06
Cl	0.07	0.08	0.07	0.09	0.86	0.88
Σ Impurities	0.76	1.5	0.8	1.21	1.46	2.13

Comparing the results of the different treatments, the amount of Pb and Cd is reduced compared to the values shown in Table 2. However, there are some treatments that are more efficient in reducing the amount of Pb, i.e., M2, M4, and M6, the three of them having in common the concentration of the reducing agent (3 wt%). On the other hand, the increase in chlorinating agent mainly produces an increase in the Cl impurities incorporated into the sample. Different carbochlorination reduction treatments do not have a strong impact on the final concentration of Fe or Mn impurities.

On the other hand, as we have seen in Section 3.2, we want to understand how the remaining impurities are distributed in the sample. Figure 7 shows the elementary composition maps of the Zn-K_α and Fe-K_α elements for the M2, M4, and M6 samples. These images show that the main element is Zn, whereas Fe is concentrated in small areas. The XRD measurements confirm that the samples are wurtzite ZnO (Figure 7d–f). However, as we have described before, we need to perform CL measurements to understand if Fe is incorporated into the ZnO lattice.

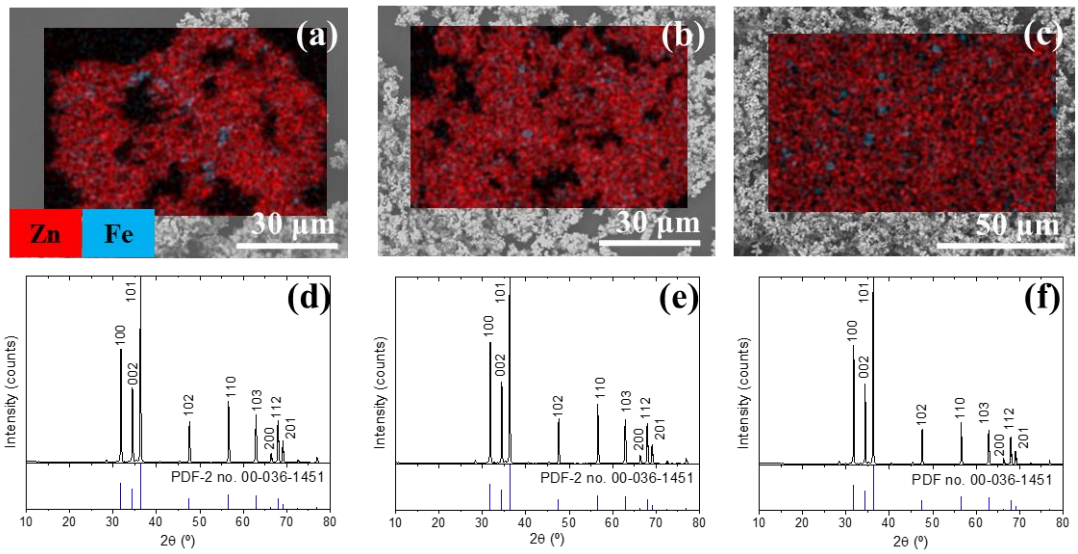

Figure 7. Compositional mappings of Zn-K_α (red) and Fe-K_α (blue) for samples (**a**) M2, (**b**) M4, and (**c**) M6. Diffractograms for samples (**d**) M2, (**e**) M4, and (**f**) M6.

Figure 8a presents the CL spectra for samples treated with fluid FET (M2, M3) and with anthracite (M4, M5) for a fixed $ZnCl_2$ amount of 2 wt%. In the case of the M2 and M3 samples, cathodoluminescence spectra show a narrow band centered around 525 nm, independently of the amount used. Additionally, the near-emission band in M2 is shifted to 405 nm. On the other hand, in the case of the M4 and M5 samples, a broad band centered at 522 nm can be appreciated, the spectra being more similar to the original WON sample.

Following the discussion in Section 3.2, the results obtained reveal that the formation of the $ZnFe_2O_4$ spinel is inhibited more when anthracite is used as a reducing agent.

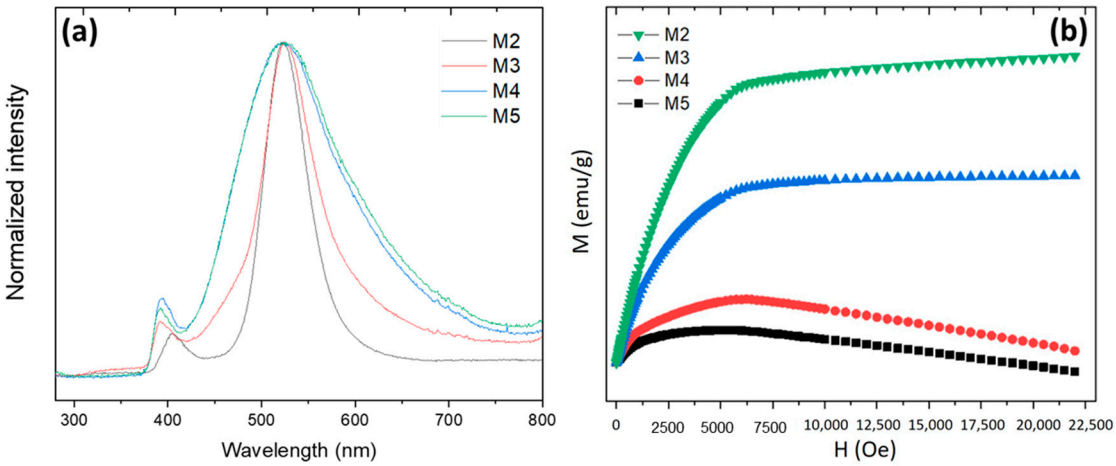

Figure 8. (**a**) CL spectra for the samples obtained using different amounts of fluid PET and anthracite as reducing agents; (**b**) VSM curves for the samples obtained using different conditions.

Figure 8b shows the VSM curves for the same four samples (M2–M5). Bulk ZnO generally exhibits diamagnetic behavior. However, it has been reported that ZnO nanoparticles are paramagnetic at room temperature. The origin of this behavior at the nanoscale is commonly associated with defects in the particles [21]. Some authors have indicated that defects such as Zn and O vacancies (V_{Zn}, V_O), oxygen interstitial (O_i), and cation interstitial (i.e., Zn_i) in a wide-gap oxide semiconductor are probably the origin of the magnetism of the ZnO nanoparticles. In fact, it is reported that the pure ZnO nanoparticles exhibited a ferromagnetic nature at room temperature due to the exchange interaction between localized electron spin moments resulting from oxygen vacancies at the surface of nanoparticles [22]. In contrast, $ZnFe_2O_4$ usually exhibits ferromagnetic behavior [23]. The VSM curves obtained for the M2 and M3 samples exhibit typical ferromagnetic behavior, where the magnetization of the samples increases with the applied magnetic field. However, the M-H curves for the M4 and M5 samples exhibit diamagnetic behavior at a high magnetic field, and weak ferromagnetic (FM) behavior in the lowest field regime. Thus, the VSM results are also in agreement with the CL observations: $ZnFe_2O_4$ and ZnO formation is favored when fluid PET and anthracite are used as reducing agents, respectively.

It should be noted that, according to the obtained results, the initial Waelz oxide is turned on more ZnO amount when anthracite is used. For this reason, the influence of the chlorination agent concentration was carried out using anthracite as the reducing agent.

To analyze the influence of the chlorinating agent amount on the carbochlorination reduction reactions, tests were carried out modifying to 3.5 wt% the amount of $ZnCl_2$ using different concentrations of anthracite as a reducing agent (3 wt% and 5 wt%, samples M6 and M7, see Table 1). The cathodoluminescence spectra registered for the M6 and M7 samples show an intense band centered at 525 nm and another band at 391 nm (Figure 9a). The CL spectrum for the M7 sample shows the broad green band typical of a ZnO compound, whereas the M6 sample shows a narrowing at the top of the band that can be attributed to $ZnFe_2O_4$ formation. Figure 9b shows the VSM curves for the M6 and M7 samples. Two different magnetic behaviors were also found, where diamagnetic and ferromagnetic behaviors at a high and low magnetic field were observed, respectively. Nevertheless, it should be noted that in the case of the M7 sample, the ferromagnetic behavior is negligible. If we compare the M7 and M5 samples, M7 exhibits a more remarkable diamagnetic behavior. Then, an increase in chlorinating agent inhibits the further formation of the spinel. Under

the experimental conditions of M7 (3.5 wt% of $ZnCl_2$ and 5 wt% of anthracite), the sample practically exhibits a diamagnetic behavior, which is typical of ZnO. Then, an increase in chlorinating agent helps to retain the ZnO lattice without the incorporation of Fe but at the expense of keeping more Pb and Cl impurities in the purified samples.

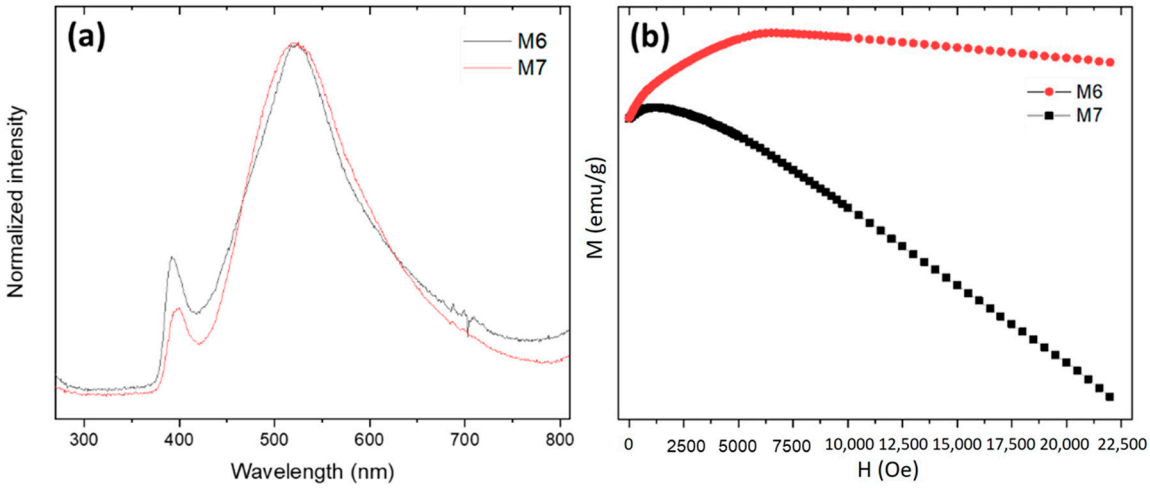

Figure 9. (**a**) CL spectra for samples obtained with 3.5 wt% of $ZnCl_2$ and 3 or 5 wt% of anthracite (M6 and M7); (**b**) VSM curves for the same samples.

4. Conclusions

The carbochlorination reduction process was investigated for the purification of the initial Waelz oxide. The influence of the reducing agent type and the amounts of both the reducing and chlorinating agents was assessed in relation to the impurities removed in the as-mentioned oxide. Both the AAS and EDX analysis shows the presence of several impurities (Fe, K, Pb, Cd, Mn, and Cl) distributed in the initial sample. XRD measurements indicate that these impurities are in the form of different lead oxides, lead chlorides, iron chlorides, and iron oxides. The micro-Raman bands registered in the initial sample can be associated with the vibration modes of ZnO, and the presence of some bands are attributable to the α-Fe_2O_3 phase. When the starting Waelz oxide subjected to pneumatic separation is exposed to a longer carbochlorination reaction time, the formation of the $ZnFe_2O_4$ phase is favored, in agreement with the CL measurements, due to the diffusion of Fe into the ZnO matrix. Regarding the type of the reducing agent, the obtained results reveal that the use of fluid-PET favored the formation of the $ZnFe_2O_4$ phase, while it is greatly inhibited when anthracite was used. Independently of the type of the reducing agent, and for a fixed chlorinating agent amount, higher impurity concentrations remain in the sample for a higher wt% of the reducing agent. The higher concentrations of $ZnCl_2$ and anthracite mostly inhibit the formation of $ZnFe_2O_4$ but at the expense of having more impurities in the purified sample. Despite that, a mixture of ZnO and $ZnFe_2O_4$ phases can be obtained with a purity higher than 98% from Waelz oxide using a carbochlorination process, with an almost complete elimination of harmful impurities (Pb, Cd).

Author Contributions: Conceptualization, F.A.L.; methodology, L.A. and B.S.; validation, L.A., B.S., P.F. and F.A.L.; formal analysis, L.A. and B.S.; investigation, L.A., B.S. and F.A.L.; resources, P.F. and F.A.L.; data curation, L.A. and B.S.; writing—original draft preparation, L.A. and B.S.; writing—review and editing, L.A., B.S., P.F. and F.A.L.; visualization, L.A. and B.S.; funding acquisition, B.S., P.F. and F.A.L. All authors have read and agreed to the published version of the manuscript.

Funding: The authors are grateful to the Comunidad de Madrid for support via the Project PR65/19-22464 (Proyectos de I+D para jóvenes doctores) and to the project CPP2022-009910 financed by MCIN/AEI/10.13039/501100011033 and by NextGeneration EU/PRTR.

Data Availability Statement: The original contributions presented in the study are included in the article, further inquiries can be directed to the corresponding authors.

Acknowledgments: The authors would like to thank the UCM CAI of X-Ray diffraction for performing the XRD measurements.

Conflicts of Interest: The authors declare no conflicts of interest.

References

1. Sinha, S.; Choudhari, R.; Mishra, D.; Shekhar, S.; Agrawal, A.; Sahu, K.K. Valorisation of Waste Galvanizing Dross: Emphasis on Recovery of Zinc with Zero Effluent Strategy. *J. Environ. Manag.* **2020**, *256*, 109985. [CrossRef]
2. Sar, S.; Sundqvist Ökvist, L.; Sparrman, T.; Engström, F.; Samuelsson, C. Characterization of Double Leached Waelz Oxide for Identification of Fluoride Mineral. *Metals* **2019**, *9*, 361. [CrossRef]
3. Antuñano, N.; Cambra, J.F.; Arias, P.L. Hydrometallurgical Processes for Waelz Oxide Valorisation—An Overview. *Process Saf. Environ. Prot.* **2019**, *129*, 308–320. [CrossRef]
4. Zoraga, M.; Yucel, T.; Ilhan, S.; Kalpakli, A. Investigation of Selective Leaching Conditions of ZnO, $ZnFe_2O_4$ and Fe_2O_3 in Electric Arc Furnace Dust in HNO_3. *J. Serbian Chem. Soc.* **2022**, *87*, 377–388. [CrossRef]
5. Anderson, A.; Mishra, B. Investigation of the Carbochlorination Process for Conversion of Cerium and Neodymium Oxides into Their Chlorides. *J. Sustain. Metall.* **2015**, *1*, 189–198. [CrossRef]
6. Buitrago, L.J.H.; Prada, I.D.; Amaral-Labat, G.; Beneduce Neto, F.; e Silva, G.F.B.L. Microstructural, Thermochemistry and Mechanical Evaluation of Self-Reducing Pellets Using Electric Arc Furnace (EAF) Dust Containing Zinc for Waelz Process. *Matéria* **2018**, *23*, e12006. [CrossRef]
7. Available online: https://www.icdd.com/Pdf-Product-Summary/ (accessed on 15 March 2025).
8. Ariza, R.; Dael, M.; Sotillo, B.; Urbieta, A.; Solis, J.; Fernández, P. Vapor-Solid Growth ZnO:ZrO_2 Micro and Nanocomposites. *J. Alloys Compd.* **2021**, *877*, 160219. [CrossRef]
9. Röder, R.; Geburt, S.; Zapf, M.; Franke, D.; Lorke, M.; Frauenheim, T.; da Rosa, A.L.; Ronning, C. Transition Metal and Rare Earth Element Doped Zinc Oxide Nanowires for Optoelectronics. *Phys. Status Solidi* **2019**, *256*, 1800604. [CrossRef]
10. Cuscó, R.; Alarcón-Lladó, E.; Ibáñez, J.; Artús, L.; Jiménez, J.; Wang, B.; Callahan, M.J. Temperature Dependence of Raman Scattering in ZnO. *Phys. Rev. B* **2007**, *75*, 165202. [CrossRef]
11. Wang, L.; Lu, X.; Han, C.; Lu, R.; Yang, S.; Song, X. Electrospun Hollow Cage-like α-Fe_2O_3 Microspheres: Synthesis, Formation Mechanism, and Morphology-Preserved Conversion to Fe Nanostructures. *CrystEngComm* **2014**, *16*, 10618–10623. [CrossRef]
12. Mansour, H.; Letifi, H.; Bargougui, R.; De Almeida-Didry, S.; Negulescu, B.; Autret-Lambert, C.; Gadri, A.; Ammar, S. Structural, Optical, Magnetic and Electrical Properties of Hematite (α-Fe_2O_3) Nanoparticles Synthesized by Two Methods: Polyol and Precipitation. *Appl. Phys. A* **2017**, *123*, 787. [CrossRef]
13. Yadav, R.S.; Kuřitka, I.; Vilcakova, J.; Urbánek, P.; Machovsky, M.; Masař, M.; Holek, M. Structural, Magnetic, Optical, Dielectric, Electrical and Modulus Spectroscopic Characteristics of $ZnFe_2O_4$ Spinel Ferrite Nanoparticles Synthesized via Honey-Mediated Sol-Gel Combustion Method. *J. Phys. Chem. Solids* **2017**, *110*, 87–99. [CrossRef]
14. Alcaraz, L.; Urbieta, A.; Rabanal, M.E.; Fernández, P.; López, F.A. Photocatalytic Activity of Electric-Arc Furnace Flue Dusts. *J. Mater. Res. Technol.* **2020**, *9*, 1261–1272. [CrossRef]
15. Xue, H.; Pan, N.; Li, M.; Wu, Y.; Wang, X.; Hou, J.G. Probing the Strain Effect on near Band Edge Emission of a Curved ZnO Nanowire via Spatially Resolved Cathodoluminescence. *Nanotechnology* **2010**, *21*, 215701. [CrossRef]
16. Mselmi, F.; Neffati, A.; Kammoun, S. Theoretical Investigation of the Cathodoluminescence Spectra of Co-Doped ZnO Nanowires. *J. Lumin.* **2018**, *198*, 124–131. [CrossRef]
17. Müller, S.; Zhou, M.; Li, Q.; Ronning, C. Intra-Shell Luminescence of Transition-Metal-Implanted Zinc Oxide Nanowires. *Nanotechnology* **2009**, *20*, 135704. [CrossRef]
18. Ogugua, S.N.; Ntwaeaborwa, O.M.; Swart, H.C. Luminescence, Structure and Insight on the Inversion Degree from Normal to Inverse Spinel in a $ZnAl_{(2-x)}Fe_x^{3+}O_4$system. *Bol. Soc. Esp. Ceram. Vidr.* **2021**, *60*, 147–162. [CrossRef]
19. Kjeldby, S.B.; Nguyen, P.D.; García-Fernández, J.; Haug, K.; Galeckas, A.; Jensen, I.J.T.; Thøgersen, A.; Vines, L. Prytz Optical Properties of $ZnFe_2O_4$ Nanoparticles and Fe-Decorated Inversion Domain Boundaries in ZnO. *Nanoscale Adv.* **2023**, *5*, 2102–2110. [CrossRef]
20. Granone, L.I.; Nikitin, K.; Emeline, A.; Dillert, R.; Bahnemann, D.W. Effect of the Degree of Inversion on the Photoelectrochemical Activity of Spinel $ZnFe_2O_4$. *Catalysts* **2019**, *9*, 434. [CrossRef]

21. Bououdina, M.; Azzaza, S.; Ghomri, R.; Shaikh, M.N.; Dai, J.H.; Song, Y.; Song, W.; Cai, W.; Ghers, M. Structural and Magnetic Properties and DFT Analysis of ZnO:(Al,Er) Nanoparticles. *RSC Adv.* **2017**, *7*, 32931–32941. [CrossRef]
22. Dasari, M.; Godavarti, U.; Mote, V. Structural, Morphological, Magnetic and Electrical Properties of Ni-Doped ZnO Nanoparticles Synthesized by Co-Precipitation Method. *Process. Appl. Ceram.* **2018**, *12*, 100–110. [CrossRef]
23. Yao, C.; Zeng, Q.; Goya, G.F.; Torres, T.; Liu, J.; Wu, H.; Ge, M.; Zeng, Y.; Wang, Y.; Jiang, J.Z. $ZnFe_2O_4$ Nanocrystals: Synthesis and Magnetic Properties. *J. Phys. Chem. C* **2007**, *111*, 12274–12278. [CrossRef]